

# Laser induced thermal-wave fields in multi-layered spherical solids based on Green function method

Jie Zhang,<sup>1</sup> Guangxi Xie,<sup>1,2</sup> Chinhua Wang,<sup>1,a)</sup> and Andreas Mandelis<sup>3</sup>

<sup>1</sup>Key Lab of Modern Optical Technologies of Jiangsu Province, Institute of Modern Optical Technologies, Soochow University, Suzhou, Jiangsu 215006, China

<sup>2</sup>Department of Physics, Jiangnan University, Wuxi, Jiangsu 214122, People's Republic of China

<sup>3</sup>Center for Advanced Diffusion-Wave Technologies (CADIFT), Department of Mechanical and Industrial Engineering, University of Toronto, M5S 3G8 Ontario, Canada

(Received 6 June 2012; accepted 6 July 2012; published online 10 August 2012)

In this paper, we establish a Green-function based theoretical model for evaluating solid multi-layered spherical samples which are illuminated by a frequency modulated incident beam. The specific Green function for the multi-layered spherical structure is derived and an analytical expression for the thermal-wave field in such a spherical sample is presented. The characteristics of the thermal-wave field with respect to the thermophysical, geometrical, and measurement parameters are presented. Unlike the quadruple method, the Green function method is capable of evaluating thermal-wave fields at any point of multi-layered structures with arbitrary intensity distributions of incident laser beams. Furthermore, experimental validation is also presented in the form of experimental results with steel spheres of various diameters. © 2012 American Institute of Physics. [<http://dx.doi.org/10.1063/1.4743011>]

## I. INTRODUCTION

Photothermal techniques have been established as a powerful tool for the thermophysical characterization and nondestructive evaluation (NDE) of a wide variety of materials.<sup>1–5</sup> Photothermal radiometry is based on the generation and detection of oscillating thermal infrared emission of a sample as a result of absorption and nonradiative conversion of an intensity modulated incident laser beam, in which infrared emission from the material can be quantitatively evaluated by the Stefan–Boltzmann law. For decades, research in photothermal techniques has been restricted to samples with flat surfaces. With the increasing applications of photothermal radiometry (PTR) to nondestructive evaluation of industrially manufactured products, requirements for characterization of samples with curvature, such as cylinders and spheres, have made it necessary to consider the formulation of thermal-wave fields in curvilinear coordinate systems. Recently, significant progress has been made on studies of samples with curved surfaces. Wang *et al.* investigated both theoretically and experimentally cylindrical and spherical samples<sup>6–10</sup> by the Green function method which is a well known formalism for solving boundary-value problems, including thermal-wave fields in diverse geometries. The thermal-wave field of a sample with incident light of arbitrary angular and/or radial intensity distribution can be obtained once the Green function is determined for a specific geometry. In parallel, Salazar *et al.* developed a technique for characterizing the thermal-wave fields of multi-layered cylindrical and spherical samples using the quadruple method,<sup>11–13</sup> in which a linear relation between temperature and incident heat flux at the outer and inner surfaces of the

sample is used to derive the thermal-wave fields of layered structures. The quadruple method, however, is limited to samples with cylindrical or spherical symmetry and can only calculate the temperature on the sample surface, which sometimes limits the general applicability of the theoretical model. In this paper, we develop a theoretical model for characterizing solid multi-layered spherical samples using the Green function method. We first develop the thermal-wave Green function for the multi-layered geometry, and then we present an analytical expression for the thermal-wave field in such a spherical solid. The earlier theoretical models<sup>8,9,11</sup> for two-layer or homogeneous spheres have been used to demonstrate the validity of this multi-layered model in the limit of two-layers. Finally, experimental validation is presented in which two spheres of different diameters are measured and fitted to the theoretical model. In contrast to the inverse-problem method, a “forward” data-fitting process<sup>14</sup> is employed to reconstruct the depth profile of the thermophysical parameter. The experimental results show good agreement with the theoretical model.

## II. THEORY

The thermal-wave field of a multi-layered spherical solid with outer radius  $r_N$  and inner radii  $r_{N-1}, r_{N-2}, \dots, r_1$ , ( $b = r_N > r_{N-1} > r_{N-2} > \dots > r_1 = a$ ) can be derived by the Green function method. The geometry and the coordinates of the boundary-value problem are shown in Figure 1. The thermal conductivity and diffusivity of regions 1 and 2, ..., N are denoted with  $(k_1, \alpha_1)$  and  $(k_2, \alpha_2), \dots, (k_N, \alpha_N)$ , respectively. The exciting laser beam, which is of circular symmetry with respect to the z axis and subtends an angle  $2\psi$ , Figure 1, impinges on the spherical surface. The harmonic thermal-wave equation for the material under investigation in region N can be written as

<sup>a)</sup>E-mail: chinhua.wang@suda.edu.cn.

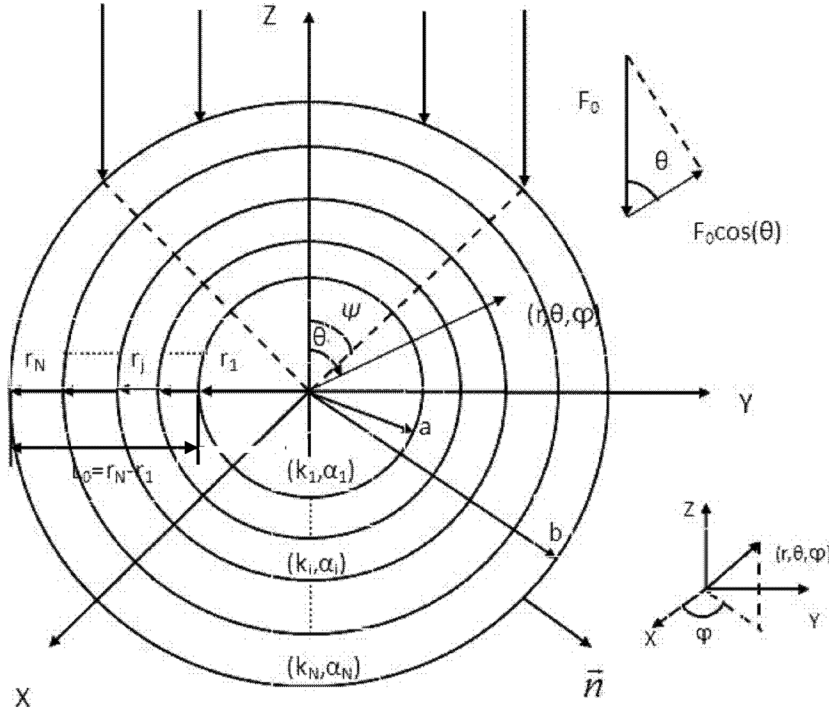


FIG. 1. The geometry and coordinates of a multi-layered spherical solid.

$$\nabla^2 T(\vec{r}, \omega) - \sigma_N^2(\omega) \cdot T(\vec{r}, \omega) = -\frac{1}{k_N} Q(\vec{r}, \omega), \quad (1)$$

where  $\sigma_N(\omega) = (i\omega/\alpha_N)^{1/2} = (1+i) \cdot \sqrt{\omega/2\alpha_N}$  is the complex thermal wave-number,  $\omega$  is the angular modulation frequency of the laser beam, and  $Q(\vec{r}, \omega)$  is the volume thermal source at coordinates  $\vec{r} = (r, \theta, \varphi)$  inside the sphere. Based on the Green function method, the general solution for Eq. (1) can be expressed as<sup>15</sup>

$$\begin{aligned} T(\vec{r}, \omega) = & \left( \frac{\alpha_N}{k_N} \right) \iiint_{V_0} Q(\vec{r}_0, \omega) \cdot G^{(N)}(\vec{r}|\vec{r}_0, \omega) \cdot dV_0 \\ & + \alpha_N \oint_{S_0} \left[ G^{(N)}(\vec{r}|\vec{r}_0^s, \omega) \cdot \vec{\nabla}_0 T(\vec{r}_0^s, \omega) \right. \\ & \left. - T(\vec{r}_0^s, \omega) \cdot \vec{\nabla}_0 G^{(N)}(\vec{r}|\vec{r}_0^s, \omega) \right] \cdot d\vec{S}_0^s, \quad (2) \end{aligned}$$

where  $S_0$  is the surface surrounding the domain volume  $V_0$  (i.e., region N), which includes the harmonic source  $Q(\vec{r}_0, \omega)$ ;  $\vec{n}$  is a unit position vector from the origin representing the coordinate of a source point on the surface  $S_0$ :  $\vec{S}_0 = \vec{n} \cdot dS_0$ ;  $\vec{r}_0^s$  is a position vector tracing the boundary surface  $S_0$ .  $G^{(N)}(\vec{r}|\vec{r}_0^s, \omega)$  is the thermal-wave Green function with units of  $[s/m^3]$ . The general case Eq. (2) can be simplified depending on specific material properties and boundary conditions imposed on the solid. For solids with high optical absorption coefficients, such as metallic samples, the volume source can be neglected ( $Q(\vec{r}_0, \omega) \equiv 0$ ). In this paper, we will focus on metallic (opaque) materials. Moreover, considering that illumination of the outer surface by a laser beam leads to optical-to-thermal energy conversion essentially at the surface and that the thermal coupling coefficient between a metallic solid and the surrounding gas (air) is on the order of  $10^{-3}$ , the adiabatic second-kind (Neumann) boundary

condition at the outer surface can be applied. Furthermore, to convert the improper Green function to a proper one which can be applied to multi-layered solids with non-homogeneous interface conditions,<sup>15</sup> we assume a third-kind boundary condition on the inner surface of region N at  $r = r_{N-1}$  as discussed below. The homogeneous boundary conditions for the appropriate Green function and inhomogeneous boundary conditions for the temperature field, respectively, can be written as

$$k_N \vec{n} \cdot \nabla G^{(N)}(\vec{r}|\vec{r}_0, \omega)|_{r=r_{N-1}} = h_{N-1} G^{(N)}(\vec{r}|\vec{r}_0, \omega)|_{r=r_{N-1}}, \quad (3a)$$

$$k_N \vec{n} \cdot \nabla G^{(N)}(\vec{r}|\vec{r}_0, \omega)|_{r=r_N} = 0, \quad (3b)$$

$$-k_N \vec{n} \cdot \nabla T(\vec{r}, \omega)|_{r=r_{N-1}} = F_{N-1}(\vec{r}, \omega) - h_{N-1} T(\vec{r}, \omega)|_{r=r_{N-1}}, \quad (4a)$$

$$k_N \vec{n} \cdot \nabla T(\vec{r}, \omega)|_{r=r_N} = F_N(\vec{r}, \omega)|_{r=r_N}. \quad (4b)$$

Here  $h_{N-1} [Wm^{-2} K^{-1}]$  is the heat transfer coefficient at the inner surface  $S_{N-1}$ ,  $F_{N-1}$ , and  $F_N$  are the heat fluxes  $[Wm^{-2}]$  imposed on the inner and outer surface, respectively. For the exterior surface of region  $j$ ,  $r = r_j$  ( $1 \leq j \leq N-2$ ), the boundary conditions can be written as

$$H_j(\vec{r}|\vec{r}_0; \omega)|_{r=r_j} = H_{j+1}(\vec{r}|\vec{r}_0; \omega)|_{r=r_j}, \quad (5a)$$

$$k_j \frac{\partial H_j(\vec{r}|\vec{r}_0; \omega)}{\partial r} \Big|_{r=r_j} = k_{j+1} \frac{\partial H_{j+1}(\vec{r}|\vec{r}_0; \omega)}{\partial r} \Big|_{r=r_j}. \quad (5b)$$

$H_j(\vec{r}|\vec{r}_0; \omega)$  is the spatial impulse-response function in region  $j$ . Therefore, in the absence of volume thermal sources in region N and in the underlying region  $N-1$ , and with the

homogeneous boundary conditions for the Green function shown in Eqs. (4a) and (4b), the general thermal-wave field represented by Eq. (2) reduces to

$$T(\vec{r}, \omega) = -\frac{\alpha_N}{k_N} \oint_{S_{N-1}} F_{N-1}(\vec{r}_0^s, \omega) \cdot G^{(N)}(\vec{r}|\vec{r}_0^s, \omega) \cdot dS_0 + \frac{\alpha_N}{k_N} \oint_{S_N} F_N(\vec{r}_0^s, \omega) \cdot G^{(N)}(\vec{r}|\vec{r}_0^s, \omega) \cdot dS_0, \quad (6)$$

where  $G^{(N)}(\vec{r}|\vec{r}_0^s, \omega)$  is the Green function for region N which must be derived so as to satisfy the appropriate boundary conditions. It should be emphasized that the condition for Eq. (2) to be reduced to Eq. (6) is that the Green function must be proper (i.e., homogeneous boundary conditions must be satisfied at all surfaces enclosing the volume  $V_0$ ).

The details of the derivation of the Green function for the specified geometry of Fig. 1 are given in the Appendix. Section I of the Appendix develops the Green function (in region N) and the spatial impulse-response functions (in region  $N-1, \dots, 2$  and 1), respectively, for a multi-layer concentric spherical structure. The relevant Green function to be used in the exterior region  $r_{N-1} \leq r \leq r_N$  is Eq. (A33). However, great care must be taken since the Green-function derivation for region N has employed a nonhomogeneous (continuity) boundary condition at  $r = r_N$ . Therefore, the

function Eq. (A33) is an improper Green function.<sup>15</sup> As a result, it cannot be applied readily to obtain the thermal-wave field in region N, because it does not satisfy the requisite homogeneous boundary condition at  $r = r_N$  to validate the field Eq. (6). A proper Green function for the equivalent exterior region N, which satisfies a homogeneous third-kind boundary condition at  $r = r_{N-1}$ , must be used instead. This Green function is given by Eq. (A55). However, in Eq. (A55), there is no direct thermal-wave coupling to the under-layer in region (N-1). There is only an indirect involvement of the inner region at thermal equilibrium through the heat transfer coefficient  $h_{N-1}$ . A direct involvement of region (N-1) into the proper Green function for region N, Eq. (A55), can be introduced through correlating the thermal parameters  $(k_{N-1}, \alpha_{N-1})$  in Eq. (A33) in region N to the (otherwise arbitrary) constant  $h_{N-1}$  in Eq. (A55). This line of reasoning leads to the equivalence relations (A57) and (A58) in Sec. II of the Appendix. Those relations show that for the specified value of  $h_{N-1}$ , the proper Green function Eq. (A55), and its integral, Eq. (6), can be used as an equivalent Green function and as a valid thermal-wave field distribution integral, respectively, to describe the effects of the multi-layer, despite the nonhomogeneous interior boundary conditions. In summary, the appropriate Green function to be used in Eq. (6) can finally be written with the observation coordinate-position vector,  $r$ , as the running variable in the form

$$G^{(N)}(\vec{r}|\vec{r}_0; \omega) = \frac{\sigma_N}{4\pi\alpha_N} \sum_{l=0}^{\infty} \frac{N_l(\theta)N_l(\theta_0)}{[Y_l(r_N) - X_l(r_{N-1})]} \times \begin{cases} [n_l(k_N r_0) - Y_l(r_N) \cdot j_l(k_N r_0)][n_l(k_N r) - X_l(r_{N-1}) \cdot j_l(k_N r)], & (r_{N-1} \leq r \leq r_0) \\ [n_l(k_N r_0) - X_l(r_{N-1}) \cdot j_l(k_N r_0)][n_l(k_N r) - Y_l(r_N) j_l(k_N r)], & (r_0 \leq r \leq r_N) \end{cases} \quad (7)$$

where  $r_0$  is the Green-function source radial location, and

$$X_l(r_{N-1}) \equiv \frac{[n'_l(k_N r_{N-1}) - m_{N-1} \cdot n_l(k_N r_{N-1})]}{[j'_l(k_N r_{N-1}) - m_{N-1} \cdot j_l(k_N r_{N-1})]}, \quad (8)$$

$$Y_l(r_N) \equiv \frac{n'_l(k_N r_N)}{j'_l(k_N r_N)}, \quad (9)$$

$$m_{N-1} = \frac{[j'_l(\kappa_{N-1} r_{N-1}) - n'_l(\kappa_{N-1} r_{N-1}) \cdot \gamma_{(N-1)}]}{\beta_{N,(N-1)} [j_l(\kappa_{N-1} r_{N-1}) + n'_l(\kappa_{N-1} r_{N-1}) \cdot \gamma_{(N-1)}]},$$

and  $\beta_{N,(N-1)} = k_N/k_{N-1}$ . (10)

Here  $k_j = i\sigma_j = -(1-i)\sqrt{\omega/2\alpha_j}$ , ( $j = 1, 2, \dots, N$ ) are thermal wave numbers.  $\gamma_{N-1} \equiv \frac{i_{11}^{(N-1)}}{i_{11}^{(N-1)}}$ , where the rhs symbols are defined in the Appendix.  $j_l(z)$ ,  $j'_l(z)$  are a spherical Bessel function of the first kind of a complex argument of order  $l$

and its derivative, and  $n_l(z)$ ,  $n'_l(z)$  are a spherical Bessel function of the second kind of a complex argument of order  $l$  and its derivative.

Also,  $N_l(\theta) = \sqrt{\frac{2l+1}{2}} P_l(\cos \theta)$ ,  $N_l(\theta_0) = \sqrt{\frac{2l+1}{2}} P_l(\cos \theta_0)$ , where  $P_l(\cos \theta)$  is a Legendre polynomial.

In view of the structure of Eq. (6), the prescribed thermal-wave fluxes  $F_{N-1}$  and  $F_N$ , at the inner and outer surface of the N-th layer, respectively, must be specified. In our case, there is no incident flux prescribed at the inner surface  $r = r_{N-1}$ , therefore,

$$F_{N-1}(\vec{r}_0, \omega) = 0, \quad (11)$$

Assuming that the incident light intensity on the exterior surface is uniform in conformity with standard experimental photothermal configurations such as laser infrared PTR (although the theoretical method is valid for any arbitrary incident beam profile), the thermal-wave flux on that surface must be weighted using a projection factor in the form of the

cosine of the incident uniform light intensity which can be expressed as

$$F_N(r_N, \theta, \varphi, \omega) = \begin{cases} \frac{1}{2}F_0 \cos \theta, & 0 \leq \theta \leq \psi, \quad 0 \leq \varphi \leq 2\pi \\ 0, & \psi \leq \theta \leq \pi, \quad 0 \leq \varphi \leq 2\pi \end{cases} \quad (12)$$

Substituting Eqs. (11) and (12) into Eq. (6), we obtain

$$T(\vec{r}, \omega) = \frac{\alpha_N F_0}{2k_N} \oint_{S_N} G^{(N)}(\vec{r}|\vec{r}^s, \omega) \cdot \cos \theta_0 \cdot dS_0, \quad (13)$$

where  $dS_0 = (2\pi r_N \sin \theta_0) \cdot (r_N \cdot d\theta_0) = 2\pi r_N^2 \sin \theta_0 d\theta_0$ . Now interchanging  $(r, \theta, \varphi) \leftrightarrow (r_0, \theta_0, \varphi_0)$  in the Green function, Eq. (7), so as to allow integrations over the source coordinates  $(r_0, \theta_0, \varphi_0)$  and letting  $r_0 = r_N$  (surface source), integration of Eq. (13) and separation of the  $l = 0$  and  $l = 1$  terms for computational convenience, yields the final thermal-wave field analytically as

$$T(\vec{r}, \omega) = \frac{F_0}{4k_N} \left\{ \frac{[n_0(\kappa_N r) - X_0(r_{N-1})j_0(\kappa_N r)]}{j'_0(\kappa_N r_N)[Y_0(r_N) - X_0(r_{N-1})]} \Big|_{l=0} \cdot \frac{\sin^2 \psi}{2} + \frac{[n_1(\kappa_N r) - X_1(r_{N-1})j_1(\kappa_N r)]}{j'_1(\kappa_N r_N)[Y_1(r_N) - X_1(r_{N-1})]} \Big|_{l=1} \cdot \cos \theta \cdot (1 - \cos^3 \psi) - \sum_{l=2}^{\infty} \frac{[n_l(\kappa_N r) - X_l(r_{N-1})j_l(\kappa_N r)]}{j'_l(\kappa_N r_N)[Y_l(r_N) - X_l(r_{N-1})]} \cdot \frac{(2l+1)\sin \psi}{(l-1)(l+2)} P_l(\cos \theta) [\sin \psi P_l(\cos \psi) + \cos \psi P_l^1(\cos \psi)] \right\} \quad (14)$$

where  $P_l, P_l^m$  are Legendre polynomials and Associated Legendre polynomials, respectively.

From the structure of this expression, it is seen that the frequency dependence of the thermal-wave field of a multi-layered sphere under illumination with a uniform light beam is a strong function of the material thermal diffusivity as well as geometrical factors of the solid.

If the exciting laser beam is Gaussian, the thermal-wave flux on that surface can be expressed as

$$F_N(r_N, \theta, \varphi, \omega) = \begin{cases} \frac{1}{2}F_0 e^{-\left(\frac{b^2 \sin^2 \theta}{w^2}\right)} \cos \theta, & 0 \leq \theta \leq \psi, \quad 0 \leq \varphi \leq 2\pi \\ 0, & \psi \leq \theta \leq \pi, \quad 0 \leq \varphi \leq 2\pi \end{cases} \quad (15)$$

Here  $b$  is the radius of the sphere, and  $w$  is the spotsize of the laser beam.

Then the harmonic thermal-wave equation for the material under investigation in region N can be written as

$$T(\vec{r}, \omega) = \frac{\alpha_N \cdot F_0}{2k_N} \oint_{S_N} G^{(N)}(\vec{r}|\vec{r}^s, \omega) \cdot e^{-\left(\frac{b^2 \sin^2 \theta}{w^2}\right)} \cdot \cos \theta_0 \cdot dS_0. \quad (16)$$

Using Eq. (7), the thermal-wave field in region N can be obtained

$$T(\vec{r}, \omega) = \left( \frac{F_0 w^2}{8k_N b^2} \right) \left\{ \frac{[n_0(\kappa_N r) - X_0(r_{N-1})j_0(\kappa_N r)]}{j'_0(\kappa_N r_N)[Y_0(r_N) - X_0(r_{N-1})]} \Big|_{l=0} \cdot \left[ 1 - e^{-\frac{b^2 \sin^2 \psi}{w^2}} \right] + \sum_{l=1}^{\infty} \frac{[n_l(\kappa_N r) - X_l(r_{N-1})j_l(\kappa_N r)]}{j'_l(\kappa_N r_N)[Y_l(r_N) - X_l(r_{N-1})]} \right. \\ \left. \times (2l+1)P_l(\cos \theta) \cdot \int_0^\psi P_l(\cos \theta_0) \cos \theta_0 \sin \theta_0 e^{-\frac{b^2 \sin^2 \psi}{w^2}} d\theta_0 \right\}. \quad (17)$$

Based on Eq. (17), the thermal-wave fields of a spherical solid with Gaussian beam illumination can be obtained readily with a numerical integration.

### III. NUMERICAL SIMULATIONS

#### A. Special cases

In this section, we will focus on verifying this theoretical model through special-case simplification and comparison. Prior to this, it is noted that although Eq. (14) gives the thermal-wave field at any point inside the sphere, using the

PTR technique with an opaque solid only the thermal-wave field from the sample surface can be detected.<sup>16</sup> Therefore, our investigations and simulations will be restricted to the sample surface at  $r = r_N$ . In all simulations, the amplitude and phase of the surface thermal-wave field are normalized to the corresponding amplitude and phase of a homogeneous flat surface of the same material with semi-infinite thickness (AISI 1018 steel). The thermophysical parameters of AISI 1018 steel are  $k = 51.9 \text{ W/mK}$ ,  $\alpha = 13.57 \times 10^{-6} \text{ m}^2/\text{s}$ .<sup>17</sup> First, if we set parameters  $(k_1, \alpha_1), (k_2, \alpha_2), \dots, (k_{N-1}, \alpha_{N-1})$  in regions 1, 2, ..., (N - 1) equal to parameters  $(k_N, \alpha_N)$  in region N, i.e.,

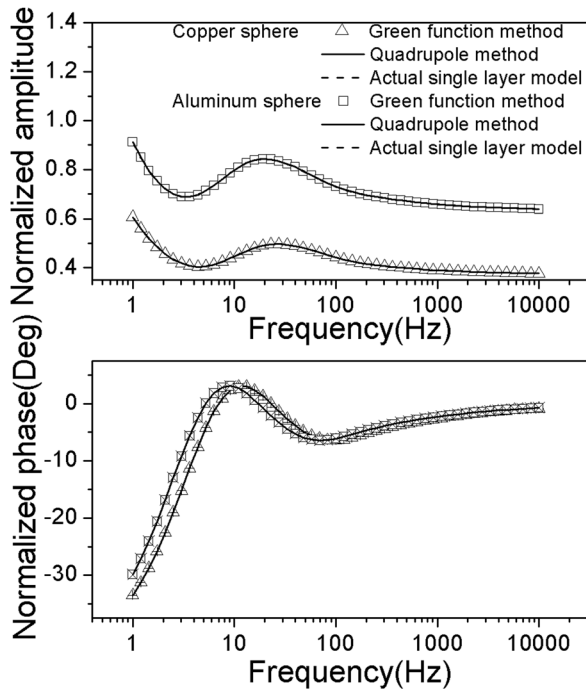


FIG. 2. The frequency dependence of thermal-wave field from solid spheres simulated by this single layer model from degeneration of Eq. (14).

$(k_1, \alpha_1) = (k_2, \alpha_2) = \dots = (k_N, \alpha_N)$ , Eq. (14) can be easily reduced to a single-layer model, i.e., a homogeneous sphere. The frequency dependence of the surface thermal-wave field of a uniform solid sphere (the North Pole point,  $\psi = \pi/2$ ) is simulated in this manner and is shown in Fig. 2. In the simulations, two spherical solids with the same diameter (4 mm) but made of different materials (aluminum and copper) are investigated in the limit where the incident light beam is large enough to cover the whole projectional surface of the spherical solid, i.e.,  $\psi = \pi/2$ . The other parameters used in the simulations are  $401 \text{ mK}$ ,  $\alpha = 112.34 \times 10^{-6} \text{ m}^2/\text{s}$  for copper and  $k = 204 \text{ W/mK}$ ,  $\alpha = 84.18 \times 10^{-6} \text{ m}^2/\text{s}$  for aluminum. In addition, the same simulations performed with the theoretical model developed in Ref. 11 are also presented for comparison. It can be seen that both amplitude and phase channel of each sample calculated with the model of Eq. (14) in the limit of a single layer and those using the actual single layer expression (the dashed line in Fig. 2) show perfect agreement. The single layer model developed in Ref. 8 has been found to be suitable for interpreting PTR measurements. In summary, the photo-thermal theoretical model of Eq. (14) for a multi-layer sphere exhibits the correct expected behavior in the limit of a single-layer sphere.

Equation (14) can also be reduced to a 2-layer model by assuming parameters  $(k_1, \alpha_1), (k_2, \alpha_2), \dots, (k_{N-2}, \alpha_{N-2})$  in region 1, 2, ...,  $(N-2)$  are equal to parameters  $(k_{N-1}, \alpha_{N-1})$  in region  $N-1$ , i.e.,  $(k_1, \alpha_1) = (k_2, \alpha_2) = \dots = (k_{N-1}, \alpha_{N-1})$ . Under the same illumination and measurement geometry, two AISI 1018 steel spheres coated with aluminum and copper, respectively are considered, with the same diameter, equal to 4 mm, and coating thickness 1 mm. The surface thermal-wave fields in the 2-layer solid sphere illuminated by modulated light were calculated and Fig. 3 shows the frequency dependencies. The symbols are results based on the

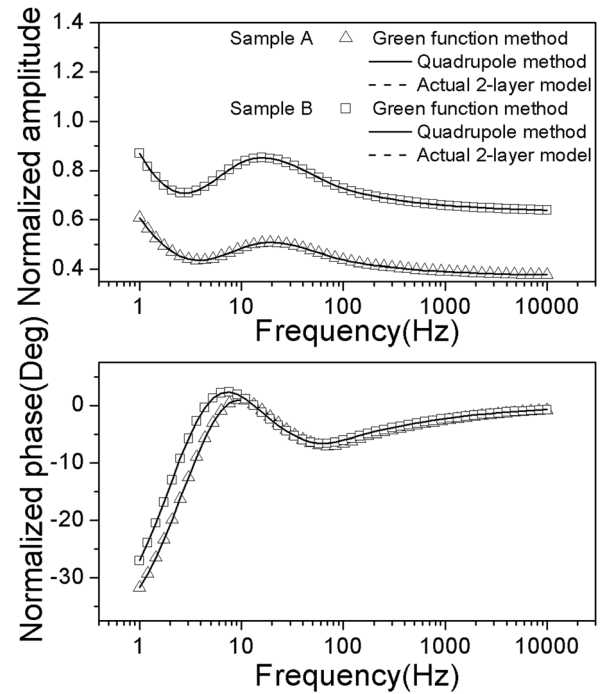


FIG. 3. The frequency dependence of surface thermal-wave field from 2-layer spherical solids. Sample A is a steel sphere coated with copper and sample B is a steel rod coated with aluminum.

present model, Eq. (14), in the limit of two layers and the solid lines were calculated using the 2-layer quadrupole method model developed in Ref. 11 for comparison. The results are identical throughout the entire frequency range. The 2-layer model developed in Ref. 9 is also presented with a dashed line in Fig. 3 and also shows perfect coincidence with the simplified case of the multi-layer model. The foregoing special cases are proof that the generalized complicated model of multi-layered spheres yields the expected results in a number of important limiting cases. Indeed, the agreement involves both our own earlier results<sup>9</sup> and those obtained with the model developed using the quadrupole method.

## B. General case

Simulations involving the full multi-layered model are now presented. Using the same illumination and measurement geometry as above, two AISI 1018 steel spheres with a 4 mm diameter and different thermal conductivity depth profiles are investigated. We assume that the radial thermal conductivity of the inhomogeneous layer in the multilayered spheres varies continuously with the depth dependence<sup>18</sup>

$$k(r) = k_0 \left( \frac{1 + \Delta e^{-Qr}}{1 + \Delta} \right)^2, \quad \text{with} \quad \Delta = \frac{1 - \sqrt{k'/k_0}}{\sqrt{k'/k_0} - e^{-QL_0}}, \quad (18)$$

where  $k_0$  and  $k'$  represent the thermal conductivity of the outermost layer and innermost layer, respectively;  $L_0$  is the total thickness of the inhomogeneous surface layer (i.e.,  $L_0 = r_N - r_1$ ). For a 2-layer sphere, only the outer layer  $r_2 \geq r \geq r_1$  is assumed inhomogeneous with depth  $L_0 = r_2 - r_1$ . The exponent  $Q$  represents the thermal gradient. The assumed depth

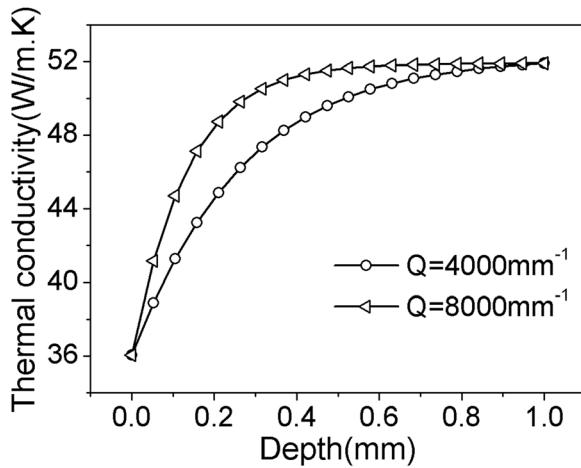


FIG. 4. The assumed thermal conductivity depth profiles of two spherical samples with different thermal gradients,  $Q$  [ $\text{mm}^{-1}$ ].

profile ansatz Eq. (18) is capable of expressing arbitrary monotonically increasing or decreasing depth profiles if parameters are properly chosen. Figure 4 shows the assumed thermal conductivity depth profiles of the two spheres. The thermal conductivity of the inhomogeneous layer is continuously increased from  $k = 36.05$  W/mK (at the surface) to the saturated value  $k' = 51.9$  W/mK at  $L_0 (= 1$  mm) inside the material but with different gradients for the two spheres;  $Q = 4000$  ( $1/\text{mm}$ ) and  $Q = 8000$  ( $1/\text{mm}$ ), respectively. Figure 5 is the comparison of the frequency dependence of the surface thermal-wave field in a sphere made of AISI 1018 steel calculated by the Green function theoretical

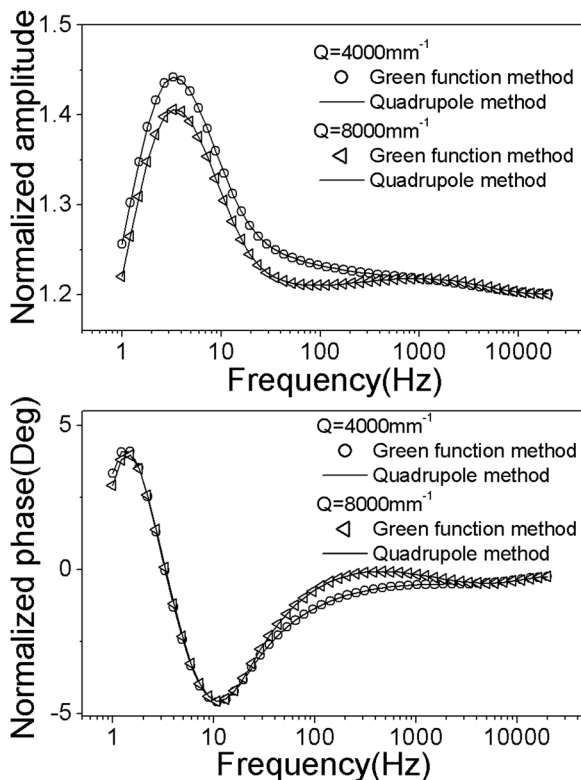


FIG. 5. Comparison of the frequency dependence of surface thermal-wave field calculated by the Green function theoretical model and by the quadrupole method.

model, Eq. (14) (symbols) and the quadrupole method (solid line) in Ref. 13. In Fig. 5, spheres with the continuously variable thermal conductivity depth profiles of Fig. 4 are considered, however, the use of the discrete multiple layer formula Eq. (18) necessitated the approximation of the continuous profile with a step profile. For each virtual slice,  $j$ ,  $1 \leq j \leq N$  (usually for  $L_0 = 1$  mm,  $N = 30$  is sufficient to describe a continuous profile) the value of  $k(r) = k(r_j)$  is calculated by using Eq. (18) in a stepwise manner for each slice with radial limits  $r_j \leq r \leq r_{j+1}$ . The frequency scans of Fig. 5 are normalized by those of a corresponding single-layer flat surface of the same material and thermal conductivity equal to 51.9 W/mK. It is further seen in Fig. 5 that both amplitude and phase curves calculated with the Green function model completely overlap those curves based on the quadrupole method over the entire frequency range. This indicates that both theoretical models are suitable for characterizing multi-layered spherical samples using the PTR technique.

As shown in Eq. (14), the thermal-wave field is also a sensitive function of the geometrical and measurement parameters. Figure 6(a) shows the normalized amplitude and phase of a spherical solid at different azimuthal angles  $\theta$  (diameter = 4 mm). Figure 6(b) shows the normalized amplitude and phase of spheres with various diameters ( $D$ ) at  $\theta = 0^\circ$ . In the simulation, the parameters  $k$ ,  $k'$ , and  $L_0$  are the same as those used in Fig. 5 and  $Q = 4000$   $\text{mm}^{-1}$ .

From Fig. 6(a), it is seen that under the same illumination and same geometrical diameter, the thermal-wave field is very sensitive to the measurement angle  $\theta$ , which suggests that precise alignment is required during an experiment. In Fig. 6(b), it is seen that the thermal-wave signal varies more rapidly at increasing frequencies when the solid diameter decreases. At very high frequencies, all normalized amplitudes and phases converge to constant values, as expected, due to the very short thermal diffusion length when compared with the radius of curvature of the sphere. At high frequencies, the normalized amplitudes are not equal (ratio  $\neq 1$ ) because the semi-infinite flat reference material is AISI 1018 steel with  $k = 51.9$  W/mK (unhardened inner material), whereas the thermal conductivity of the surface of the inhomogeneous layer is 36.05 W/mK (hardened surface).

Finally, we present the thermal-wave field of a surface illuminated by a Gaussian laser beam. In the simulation, the diameter of all spheres is assumed to be 10 mm, and the spot-size  $w$  is assumed to be 2 mm, 4 mm, 10 mm, and 5000 mm (i.e., close to infinite), respectively. The parameters of the profile of the thermal conductivity of the inhomogeneous layer are  $Q = 4000$   $\text{mm}^{-1}$ ,  $L_0 = 1$  mm. The simulation results are shown in Fig. 7. It is seen that as the spot-size increases, both amplitude and phase converge to the response of spheres illuminated with a homogeneous beam. When the laser spot-size  $W = 500$  mm, the two lines overlap, as expected, because the beam spatial profile distribution converges to a uniform distribution. The Green-function sensitivity to beam spot-size demonstrates the capability of this mathematical approach to deal with arbitrary incident beam profiles. Compared with the Green function method, the quadrupole approach is limited to samples with cylindrical or spherical symmetry and can only calculate the temperature on the sample surface, which

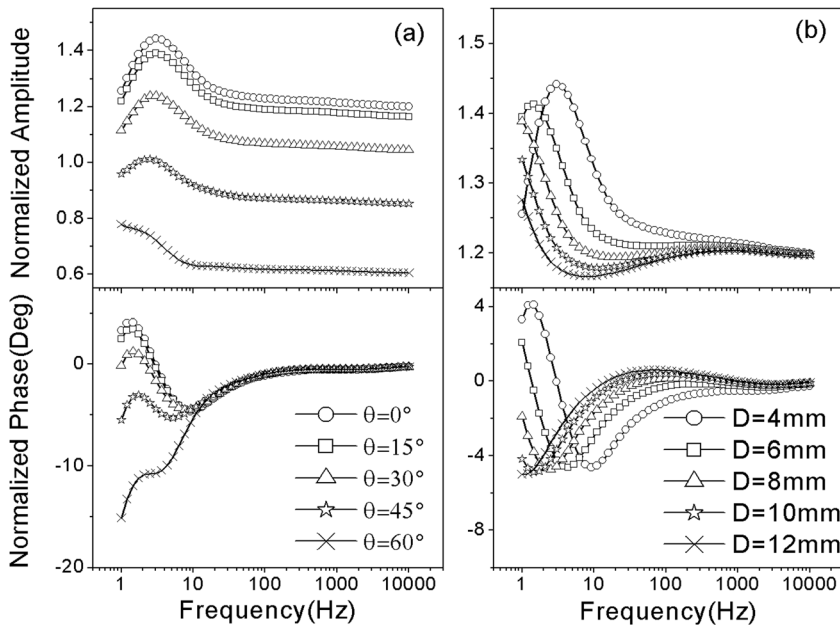


FIG. 6. (a) The normalized amplitude and phase at different azimuthal angles  $\theta$ . (b) The normalized amplitude and phase of spherical solids with different diameters at  $\theta=0^\circ$ .

sometimes limits the general applicability of this theoretical approach. Using the Green-function method, the temperature fields of arbitrary asymmetrical solids, such as wedges, as well as the thermal-wave values at any point inside the solid can be calculated.

**IV. EXPERIMENTAL AND RESULTS**

The experimental PTR setup is shown in Fig. 8. The optical excitation source was a high-power semiconductor

laser, the emitted power of which was modulated by a periodic current driver. The harmonic infrared radiation from the sample surface was collected by an off-axis paraboloidal mirror system and detected by a HgCdTe detector (EG&G Judson). The signal from the detector was pre-amplified and then fed into a lock-in amplifier (EG&G Instruments) interfaced with a personal computer.

Fabricating a multilayered or an inhomogeneous spherical solid, in practice, is actually not easy, especially when the thickness of the surface layer is on the order of tens of micrometers to millimeters. In this experiment, we used two homogeneous steel spheres with diameters of 4.998 mm and 7.138 mm as experimental samples. The well-documented surface roughness of spherical steel samples was considered to be the inhomogeneous layer for the purposes of illustrating this theoretical function. In order to eliminate the instrumental transfer function the experimental data were normalized with the data from a C1018 steel flat surface.

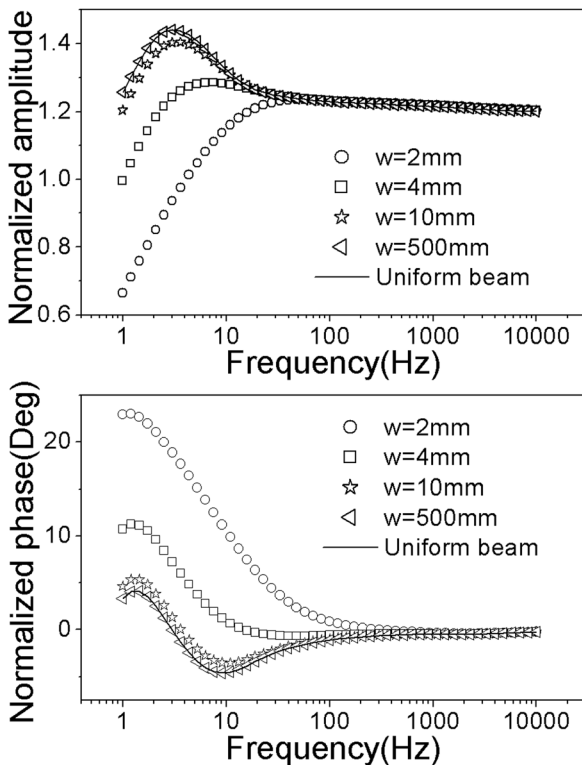


FIG. 7. Frequency dependence of the surface thermal-wave field from multilayered spheres illuminated by Gaussian beams of various spotsizes. The curves are normalized with a single-layer flat surface of the same material and conductivity equal to 51.9 W/mK.

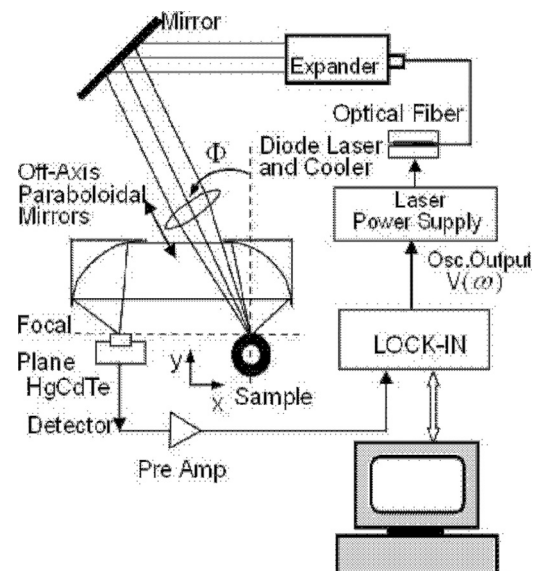


FIG. 8. The experimental PTR setup.

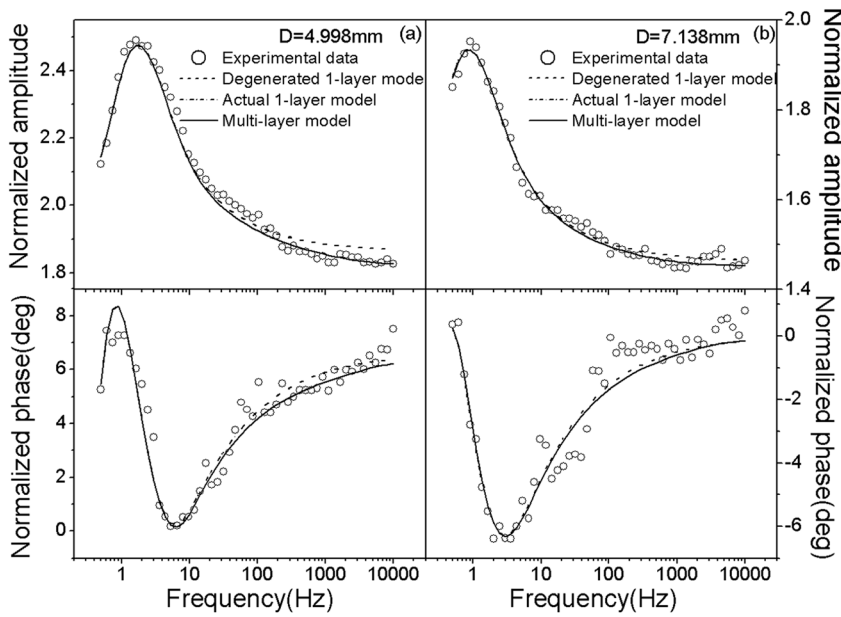


FIG. 9. Fitted results of amplitude and phase for spherical steel samples with diameters of (a) 4.998 mm and (b) 7.138 mm by one-layer and multi-layer model, respectively.

The experimental procedure has presented in Ref. 8. The samples were made of SAE52100 steel with composition: C 0.95%–1.05%, Cr 1.40%–1.65%, Si 0.15%–0.35%, P 0.025%, S 0.025%, Cu 0.25%, and Ni 0.30%.

Considering that the thickness of the surface roughness (or surface inhomogeneous layer) may be on the order of micrometers, the samples can be evaluated with the homogeneous (1-layer), or with the multi-layer model with different approximations. In Sec. III, it was shown that the multi-layer model can be reduced to the one-layer model by setting  $(k_1, \alpha_1) = (k_2, \alpha_2) = \dots = (k_N, \alpha_N)$ . In the following, we use this degenerate one-layer and the general multi-layer model, respectively, to fit the experimental data.

The experimental data and fitting curves are shown in Fig. 9. Best fits were performed with the degenerate one-layer model obtained from the multi-layer model, and also directly using the multi-layer model. The results are shown in Table I and the reconstructed thermal diffusivity depth profiles using the multi-layer model with various diameters are shown in Fig. 10. When these two types of best-fit results are compared with those from the original one-layer model,<sup>8</sup> they are found to be identical.

For the steel sphere with diameter of 4.998 mm, the best-fit results from the direct multi-layer model are:  $\alpha_1 = 12.8 \times 10^{-6} \text{ m}^2/\text{s}$ ,  $\alpha_N = 12.3 \times 10^{-6} \text{ m}^2/\text{s}$ ,  $L_0 = 56 \text{ }\mu\text{m}$ ,  $Q = 40 \text{ 600 mm}^{-1}$ , and  $\theta = 21.3^\circ$ . Compared with the results  $\alpha_1 = 12.9 \times 10^{-6} \text{ m}^2/\text{s}$ ,  $\theta = 20^\circ$  obtained with the direct

one-layer model of Ref. 8, the difference of the thermal diffusivity of the spherical substrate is small, about 0.6%. This is so because the contribution of the inhomogeneous layer to the PTR signal is very small due to the small thickness of the very thin layer. The thermal contribution of the surface thin layer modifies the signal mostly in the high frequency range, as expected. Nevertheless, taking into account the thin inhomogeneous layer of the theoretical model yields better theoretical fits than that with the one-layer model. This can be seen in Fig. 9(a), as the solid line crosses over more experimental data than the dashed line, especially in the high frequency range.

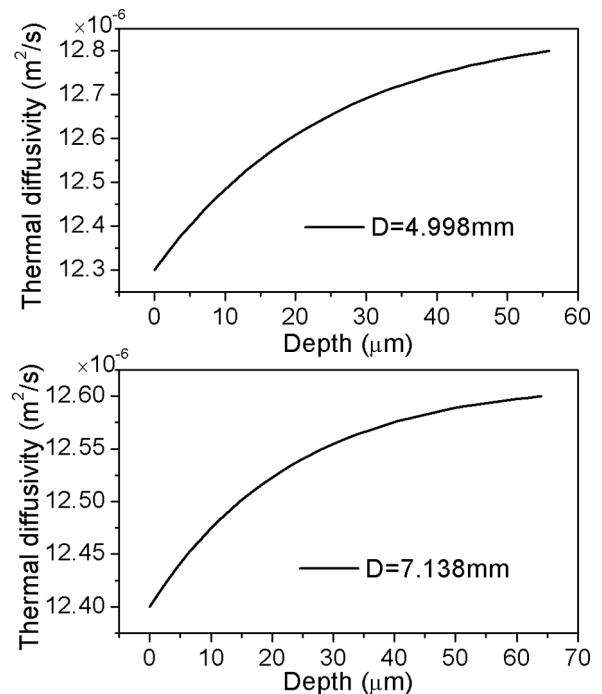


FIG. 10. Reconstructed depth profiles of thermal diffusivity of the surface roughness (or inhomogeneity) layer of two spheres with diameters of 4.998 mm and 7.138 mm.

TABLE I. Best-fitted results of spheres based on the degenerate multi-layer model of Eq. (14).

	Diameter (mm)	$\alpha_1$ ( $\text{m}^2/\text{s}$ )	$\alpha_N$ ( $\text{m}^2/\text{s}$ )	$L_0$ ( $\mu\text{m}$ )	$Q$ ( $\text{mm}^{-1}$ )	$\phi$ (Degree)
One-layer model	4.998	$12.9 \times 10^{-6}$				20
	7.138	$12.6 \times 10^{-6}$				29
Multi-layer model	4.998	$12.8 \times 10^{-6}$	$12.3 \times 10^{-6}$	56	40600	21.3
	7.138	$12.6 \times 10^{-6}$	$12.4 \times 10^{-6}$	64	43000	28.7

The same trends can also be seen for the spherical sample with diameter of 7.138 mm. The best-fit results from the direct multi-layer model are:  $\alpha_1 = 12.6 \times 10^{-6} \text{ m}^2/\text{s}$ ,  $\alpha_N = 12.4 \times 10^{-6} \text{ m}^2/\text{s}$ ,  $L_0 = 64 \text{ }\mu\text{m}$ ,  $Q = 43\,000 \text{ mm}^{-1}$ , and  $\theta = 28.7^\circ$ . Compared with the results  $\alpha_1 = 12.6 \times 10^{-6} \text{ m}^2/\text{s}$ ,  $\theta = 29^\circ$  obtained with the one-layer model of Ref. 8, the thermal diffusivities of the spherical substrate are identical. The thickness of the surface roughness is approximately the same as that of the 4.998-mm diameter sample. Similarly, the best-fit curve (solid line) from the multi-layer model, Fig. 9(b), crosses over more experimental data than that resulting from the original one-layer model (dashed line).

From the comparison of the best-fitted results using the one-layer and the multi-layer models, it can be seen that the difference between the results are very small due to the small thickness of the surface layer. This means that both models are suitable for thermal parameter measurements in this case. It is seen, however, that we can obtain more accurate results by taking into account the roughness layer and using the multi-layer model. This demonstrates the value of the multi-layer model in treating more general multi-layer spherical cases.

## V. CONCLUSIONS

We have developed a theoretical thermal-wave model that is suitable for characterizing opaque multi-layered spherical samples using optical heating from a laser beam with arbitrary intensity spatial profile. Based on the Green function method, the thermal-wave field from a multi-layered spherical sample with uniform surface illumination was obtained as a special case of spatial heating profile. The thermal-wave dependencies on various thermophysical and geometrical parameters were also investigated. Together with our earlier investigations on composite cylindrical solids and spherical solids, this work complements the applications of thermal-wave techniques, and PTR in particular, in these two most commonly used curvilinear coordinate systems. With the advantages of the Green-function method regarding the arbitrariness of the photothermal source spatial profile and its ability to handle both homogeneous boundary conditions (proper Green function) and inhomogeneous boundary conditions (improper Green function), this model offers a general analytical tool for characterizing spherical solids photothermally excited with incident laser beams of varying spot sizes and angles of incidence, two parameters of direct experimental relevance.

## ACKNOWLEDGMENTS

This work was supported by a grant from the National Natural Science Foundation of China Contract No. 60877063, Scientific Research Foundation for Returned Scholars, Ministry of Education of China, and the project of the Priority Academic Program Development (PAPD) of Jiangsu Higher Education Institutions. The Canada Research Chairs and the Natural Sciences and Engineering Research Council of Canada are gratefully acknowledged for their support through a CRC Tier I award and a Discovery Grant, respectively, to A.M.

## APPENDIX: THERMAL-WAVE GREEN FUNCTION FOR A MULTI-LAYERED SPHERICAL STRUCTURE

To calculate the Green function for a multi-layered sphere with non-homogeneous boundary conditions at the interface between the outer and inner layers, the following two related problems must be solved.

### 1. Green function and spatial impulse-response functions for a multi-layered sphere with a spatially impulsive time-harmonic thermal-wave source at $(r_0, \theta_0, \varphi_0)$ , $r_{N-1} \leq r_0 \leq r_N$ . A homogeneous Neumann condition is prescribed at $r = r_N$ .

In region  $j$  [ $j = 1, 2, \dots, (N-1)$ ], with thermophysical properties  $(k_j, \alpha_j)$ , the spatial impulse-response function  $H_j(\vec{r}|\vec{r}_0; \omega)$  (not a Green function in the layer which does not include the thermal-wave Dirac delta-function source),<sup>15</sup> satisfies the homogeneous equation

$$\begin{aligned} & \frac{1}{r} \frac{\partial^2}{\partial r^2} [rH_j(\vec{r}|\vec{r}_0; \omega)] + \frac{1}{r^2 \sin^2 \theta} \frac{\partial}{\partial \theta} \left[ \sin \theta \frac{\partial}{\partial \theta} H_j(\vec{r}|\vec{r}_0; \omega) \right] \\ & + \frac{1}{r^2 \sin^2 \theta} \frac{\partial^2}{\partial \phi^2} H_j(\vec{r}|\vec{r}_0; \omega) - \sigma_j^2(\omega) H_j(\vec{r}|\vec{r}_0; \omega) \\ & = 0 \quad (r_{j-1} \leq r \leq r_j). \end{aligned} \quad (\text{A1})$$

In region N ( $r_{N-1} \leq r \leq r_N$ ), with thermophysical properties  $(k_N, \alpha_N)$ , the Green function  $G^{(N)}(\vec{r}|\vec{r}_0; \omega)$  satisfies<sup>15</sup>

$$\begin{aligned} & \frac{1}{r} \frac{\partial^2}{\partial r^2} [rG^{(N)}(\vec{r}|\vec{r}_0; \omega)] + \frac{1}{r^2 \sin^2 \theta} \frac{\partial}{\partial \theta} \left[ \sin \theta \frac{\partial}{\partial \theta} G^{(N)}(\vec{r}|\vec{r}_0; \omega) \right] \\ & + \frac{1}{r^2 \sin^2 \theta} \frac{\partial^2}{\partial \phi^2} G^{(N)}(\vec{r}|\vec{r}_0; \omega) - \sigma_N^2(\omega) G^{(N)}(\vec{r}|\vec{r}_0; \omega) \\ & = - \frac{\delta(r - r_0) \delta(\cos \theta - \cos \theta_0) \delta(\varphi - \varphi_0)}{\alpha_N r^2} \\ & \times (r_{N-1} \leq r \leq r_N), \end{aligned} \quad (\text{A2})$$

where  $\sigma_j = (1 - i) \sqrt{\omega/2\alpha_j}$ , ( $j = 1, 2, \dots, N$ ) is the complex thermal-wave number. The Dirac delta function can now be expanded in the basis of the orthogonal eigenfunction complete set of spherical harmonics  $\{Y_{jm}(\theta, \varphi)\}$

$$\delta(\cos \theta - \cos \theta_0) \delta(\varphi - \varphi_0) = \sum_{l=0}^{\infty} \sum_{m=-l}^l Y_{lm}(\theta, \varphi) Y_{lm}^*(\theta_0, \varphi_0). \quad (\text{A3a})$$

when the exciting laser beam is of circular symmetry with respect to the  $z$  axis,  $m = 0$  (always the case in this paper). Equation (A3) reduces to

$$\delta(\cos \theta - \cos \theta_0) \delta(\varphi - \varphi_0) = \frac{1}{2\pi} \sum_{l=0}^{\infty} N_l(\theta) N_l(\theta_0), \quad (\text{A3}')$$

where  $N_l(\theta) = \sqrt{(2l+1)/2} P_l \cos(\theta)$  and  $P_l \cos(\theta)$  is a Legendre polynomial.

Both the Green function in region  $N$  and the impulse-response function in region  $j$  [ $j = 1, 2, \dots, (N - 1)$ ] can be expanded in the basis of the complete set of spherical harmonic functions  $\{Y_{jm}(\theta, \varphi)\}$

$$H_j(\vec{r}|\vec{r}_0; \omega) = \frac{1}{2\pi} \sum_{l=0}^{\infty} h_{jl}(\vec{r}|\vec{r}_0; \omega) \cdot N_l(\theta)N_l(\theta_0), \quad (\text{A4})$$

$$G^{(N)}(\vec{r}|\vec{r}_0; \omega) = \frac{1}{2\pi} \sum_{l=0}^{\infty} g_l^{(N)}(\vec{r}|\vec{r}_0; \omega) \cdot N_l(\theta)N_l(\theta_0). \quad (\text{A5})$$

Substituting Eqs. (A4) into (A1), we obtain

$$h_{jl}(r, r_0; \omega) = a_j j_l(\kappa_j r) + b_j n_l(\kappa_j r) \times (r_{j-1} \leq r \leq r_j, j = 1, r_{j-1} \equiv 0), \quad (\text{A6})$$

where  $1 \leq j \leq N - 1, j$  is natural number.

$\kappa_j(\omega) \equiv i\sigma_j = -(1 - i)\sqrt{\omega/2\alpha_j}, (j = 1, 2, \dots, N)$  and when  $j = 1, b_{1l} \equiv 0$  (because  $n_l(\kappa_1 r)$  becomes unbounded as  $r \rightarrow 0$ ).

Substituting Eqs. (A5) and (A3') into Eq. (A2), we obtain

$$\frac{1}{r} \frac{d^2}{dr^2} [r g_l^{(N)}(r|r_0; \omega)] + \left[ \kappa_N^2 - \frac{l(l+1)}{r^2} \right] g_l^{(N)}(r|r_0; \omega) = -\frac{\delta(r - r_0)}{\alpha_N r^2} (r_{N-1} \leq r \leq r_N), \quad (\text{A7})$$

when  $r \neq r_0$ , Eq. (A7) reduces to a homogenous equation. Assuming its solution to be

$$g_l^{(N)}(r, r_0; \omega) = \begin{cases} a_N j_l(\kappa_N r) + b_N n_l(\kappa_N r), & (r_{N-1} \leq r \leq r_0) \\ a_N j_l(\kappa_N r) + b_N n_l(\kappa_N r) + \frac{j_l(\kappa_N r)n_l(\kappa_N r_0) - j_l(\kappa_N r_0)n_l(\kappa_N r)}{f(r_0)W(\kappa_N r_0)} & (r_0 \leq r \leq r_N), \end{cases} \quad (\text{A8})$$

where, using Green-function reciprocity,  $W(\kappa_N r_0) \equiv j_l(\kappa_N r_0)n'_l(\kappa_N r_0) - j'_l(\kappa_N r_0)n_l(\kappa_N r_0)$  is the Wronskian identity for the functions  $j_l(\kappa_N r)$  and  $n_l(\kappa_N r), f(r_0) = \alpha_N r_0^2$ . The next task is to derive relations among the coefficients of these  $N$  equations.

In the exterior surface of region  $j, r = r_j (1 \leq j \leq N - 2)$

$$H_j(\vec{r}|\vec{r}_0; \omega)|_{r=r_j} = H_{j+1}(\vec{r}|\vec{r}_0; \omega)|_{r=r_j}, \quad (\text{A9})$$

$$k_j \frac{\partial H_j(\vec{r}|\vec{r}_0; \omega)}{\partial r} \Big|_{r=r_j} = k_{j+1} \frac{\partial H_{j+1}(\vec{r}|\vec{r}_0; \omega)}{\partial r} \Big|_{r=r_j}. \quad (\text{A10})$$

At  $r = r_N$ , a homogeneous Neumann condition is assumed

$$\frac{\partial G^{(N)}(\vec{r}|\vec{r}_0; \omega)}{\partial r} \Big|_{r=r_N} = 0. \quad (\text{A11})$$

Substituting the boundary conditions (A9)–(A11) into Eqs. (A6) and (A8), and omitting the subscript  $l$  of the coefficients for convenience, we obtain

At  $r = r_1$ ,

$$a_1 j_l(\kappa_1 r_1) = a_2 j_l(\kappa_2 r_1) + b_2 n_l(\kappa_2 r_1), \quad (\text{A12})$$

$$a_1 j'_l(\kappa_1 r_1) = \beta_{21} [a_2 j'_l(\kappa_2 r_1) + b_2 n'_l(\kappa_2 r_1)], \quad (\text{A13})$$

where

$$\beta_{j+1,j} \equiv k_{j+1}/k_j. \quad (\text{A13a})$$

At  $r = r_2$ ,

$$a_2 j_l(\kappa_2 r_2) + b_2 n_l(\kappa_2 r_2) = a_3 j_l(\kappa_3 r_2) + b_3 n_l(\kappa_3 r_2), \quad (\text{A14})$$

$$a_2 j'_l(\kappa_2 r_2) + b_2 n'_l(\kappa_2 r_2) = \beta_{32} [a_3 j'_l(\kappa_3 r_2) + b_3 n'_l(\kappa_3 r_2)], \quad (\text{A15})$$

.....

At  $r = r_j$ ,

$$a_j j_l(\kappa_j r_j) + b_j n_l(\kappa_j r_j) = a_{j+1} j_l(\kappa_{j+1} r_j) + b_{j+1} n_l(\kappa_{j+1} r_j), \quad (\text{A16})$$

$$a_j j'_l(\kappa_j r_j) + b_j n'_l(\kappa_j r_j) = \beta_{j+1,j} [a_{j+1} j'_l(\kappa_{j+1} r_j) + b_{j+1} n'_l(\kappa_{j+1} r_j)], \quad (\text{A17})$$

.....

where  $1 \leq j \leq N - 1$ .

At  $r = r_N$ ,

$$a_N j'_l(\kappa_N r_N) + b_N n'_l(\kappa_N r_N) = -\frac{\kappa_N}{\alpha_N} [j'_l(\kappa_N r_N)n_l(\kappa_N r_0) - j_l(\kappa_N r_0)n'_l(\kappa_N r_N)]. \quad (\text{A18})$$

To solve these equations, two steps are required. First, we consider  $a_1$  to be a known number. Next we turn every two equations into a pair for  $(a_j, b_j): (a_1, b_1 = 0) \rightarrow (a_2, b_2) \rightarrow \dots, (a_{N-1}, b_{N-1}) \rightarrow (a_N, b_N)$ . Then  $a_N, b_N$  can be expressed in terms of  $a_1$ , successively through the use of matrix methods applied to the pair of Eqs. (A16) and (A17), taking into account Eqs. (A12)–(A18). We thus obtain

$$\begin{bmatrix} a_2 \\ b_2 \end{bmatrix} = T_1 \begin{bmatrix} a_1 \\ b_1 \end{bmatrix}, \tag{A19}$$

$$\begin{bmatrix} a_3 \\ b_3 \end{bmatrix} = T_2 \begin{bmatrix} a_2 \\ b_2 \end{bmatrix}, \tag{A20}$$

$$\begin{bmatrix} a_4 \\ b_4 \end{bmatrix} = T_3 \begin{bmatrix} a_3 \\ b_3 \end{bmatrix}, \tag{A21}$$

.....,

$$\begin{bmatrix} a_j \\ b_j \end{bmatrix} = T_{j-1} \begin{bmatrix} a_{j-1} \\ b_{j-1} \end{bmatrix}, \tag{A22}$$

.....,

$$\begin{bmatrix} a_N \\ b_N \end{bmatrix} = T_{N-1} \begin{bmatrix} a_{N-1} \\ b_{N-1} \end{bmatrix},$$

Combining matrices yields

$$\begin{bmatrix} a_N \\ b_N \end{bmatrix} = T_{N-1} T_{N-2} \cdots T_2 T_1 \begin{bmatrix} a_1 \\ b_1 \end{bmatrix} \tag{A23}$$

and  $b_1 \equiv 0$ ,  $T_j = B_j^{-1} A_j$ , we find

$$A_j = \begin{bmatrix} j_l(\kappa_j r_j), n_l(\kappa_j r_j) \\ j'_l(\kappa_j r_j), n'_l(\kappa_j r_j) \end{bmatrix},$$

$$B_j = \begin{bmatrix} j_l(\kappa_{j+1} r_j), n_l(\kappa_{j+1} r_j) \\ \beta_{j+1,j} j'_l(\kappa_{j+1} r_j), \beta_{j+1,j} n'_l(\kappa_{j+1} r_j) \end{bmatrix}. \tag{A24}$$

Since we are only interested in  $a_N, b_N$ , we can avoid solving for  $a_1$ . In principle, we can write out the matrix  $T_{N-1} T_{N-2} \cdots T_2 T_1$ , in the form of

$$T_{N-1} T_{N-2} \cdots T_2 T_1 \equiv \begin{bmatrix} t_{11}^{(N)}, t_{12}^{(N)} \\ t_{21}^{(N)}, t_{22}^{(N)} \end{bmatrix}, \tag{A25}$$

so that,  $a_N = t_{11}^{(N)} a_1, b_N = t_{21}^{(N)} a_1$ .

It follows that

$$\frac{b_N}{a_N} = \frac{t_{21}^{(N)}}{t_{11}^{(N)}} \equiv \gamma_N, \quad \text{where} \quad \gamma_j \equiv \frac{t_{21}^{(j)}}{t_{11}^{(j)}}. \tag{A25a}$$

Also

$$a_N j'_l(\kappa_N r_N) + b_N n'_l(\kappa_N r_N) = -\frac{\kappa_N}{\alpha_N} [j'_l(\kappa_N r_N) n_l(\kappa_N r_0) - j_l(\kappa_N r_0) n'_l(\kappa_N r_N)] \tag{A26}$$

or

$$a_N [j'_l(\kappa_N r_N) t_{11}^{(N)} + n'_l(\kappa_N r_N) t_{21}^{(N)}] = \frac{\kappa_N t_{11}^{(N)}}{\alpha_N} [j'_l(\kappa_N r_N) n_l(\kappa_N r_0) - j_l(\kappa_N r_0) n'_l(\kappa_N r_N)]. \tag{A27}$$

Finally, we obtain the solution

$$a_N = \frac{\kappa_N t_{11}^{(N)}}{\alpha_N [j'_l(\kappa_N r_N) t_{11}^{(N)} + n'_l(\kappa_N r_N) t_{21}^{(N)}] \times [j_l(\kappa_N r_0) n'_l(\kappa_N r_N) - j'_l(\kappa_N r_N) n_l(\kappa_N r_0)]}, \tag{A28}$$

$$b_N = \frac{\kappa_N t_{21}^{(N)}}{\alpha_N [j'_l(\kappa_N r_N) t_{11}^{(N)} + n'_l(\kappa_N r_N) t_{21}^{(N)}] \times [j_l(\kappa_N r_0) n'_l(\kappa_N r_N) - j'_l(\kappa_N r_N) n_l(\kappa_N r_0)]}, \tag{A29}$$

Using the Green function definition

$$g^{(N)}_l(r, r_0; \omega) = \begin{cases} g_l^<(r, r_0; \omega), & (r_{N-1} \leq r \leq r_0) \\ g_l^>(r, r_0; \omega), & (r_0 \leq r \leq r_N). \end{cases} \tag{A30}$$

we find

$$g_l^<(r, r_0; \omega) = \frac{\kappa_N [j_l(\kappa_N r) t_{11}^{(N)} + n_l(\kappa_N r) t_{21}^{(N)}]}{\alpha_N [j'_l(\kappa_N r_N) t_{11}^{(N)} + n'_l(\kappa_N r_N) t_{21}^{(N)}] \times [j_l(\kappa_N r_0) n'_l(\kappa_N r_N) - j'_l(\kappa_N r_N) n_l(\kappa_N r_0)] \times (r_{N-1} \leq r \leq r_0)}, \tag{A31}$$

$$g_l^>(r, r_0; \omega) = \frac{\kappa_N [j_l(\kappa_N r_0) t_{11}^{(N)} + n_l(\kappa_N r_0) t_{21}^{(N)}]}{\alpha_N [j'_l(\kappa_N r_N) t_{11}^{(N)} + n'_l(\kappa_N r_N) t_{21}^{(N)}] \times [j_l(\kappa_N r) n'_l(\kappa_N r_N) - j'_l(\kappa_N r) n_l(\kappa_N r)]}, \tag{A32}$$

$(r_0 \leq r \leq r_N)$

where  $t_{11}^{(N)}, t_{21}^{(N)}$  are defined in Eq. (A25). Connecting this formalism to Eq. (A5)

$$G^{(N)}_l(r, r_0; \omega) = \begin{cases} G_l^<(r, r_0; \omega), & (r_{N-1} \leq r \leq r_0) \\ G_l^>(r, r_0; \omega), & (r_0 \leq r \leq r_N), \end{cases} \tag{A33}$$

where

$$G_l^<(r, r_0; \omega) = \sum_{l=0}^{\infty} N_l(\theta) N_l(\theta_0) \times \frac{\kappa_N [j_l(\kappa_N r) t_{11}^{(N)} + n_l(\kappa_N r) t_{21}^{(N)}]}{2\pi \alpha_N [j'_l(\kappa_N r_N) t_{11}^{(N)} + n'_l(\kappa_N r_N) t_{21}^{(N)}] \times [j_l(\kappa_N r_0) n'_l(\kappa_N r_N) - j'_l(\kappa_N r_N) n_l(\kappa_N r_0)]}, \tag{A34}$$

$r_{N-1} \leq r \leq r_0$

$$G_l^>(r, r_0; \omega) = \sum_{l=0}^{\infty} N_l(\theta) N_l(\theta_0) \times \frac{\kappa_N [j_l(\kappa_N r_0) t_{11}^{(N)} + n_l(\kappa_N r_0) t_{21}^{(N)}]}{2\pi \alpha_N [j'_l(\kappa_N r_N) t_{11}^{(N)} + n'_l(\kappa_N r_N) t_{21}^{(N)}] \times [j_l(\kappa_N r) n'_l(\kappa_N r_N) - j'_l(\kappa_N r) n_l(\kappa_N r)]}, \tag{A35}$$

$(r_0 \leq r \leq r_N)$

It is noted that when  $N = 2$ , from Eq. (A24)

$$\begin{aligned}
 B_1^{-1}A_1 &= \frac{\kappa_2 r_1^2}{\beta_{21}} \begin{bmatrix} \beta_{21} n'_l(\kappa_2 r_1), -n_l(\kappa_2 r_1) \\ -\beta_{21} j'_l(\kappa_2 r_1), j_l(\kappa_2 r_1) \end{bmatrix} \begin{bmatrix} j_l(\kappa_1 r_1), n_l(\kappa_1 r_1) \\ j'_l(\kappa_1 r_1), n'_l(\kappa_1 r_1) \end{bmatrix} \\
 &= c \begin{bmatrix} \beta_{21} n'_l(\kappa_2 r_1) j_l(\kappa_1 r_1) - n_l(\kappa_2 r_1) j'_l(\kappa_1 r_1), & \beta_{21} n'_l(\kappa_2 r_1) n_l(\kappa_1 r_1) - n_l(\kappa_2 r_1) n'_l(\kappa_1 r_1) \\ -[\beta_{21} j'_l(\kappa_2 r_1) j_l(\kappa_1 r_1) - j_l(\kappa_2 r_1) j'_l(\kappa_1 r_1)], & -[\beta_{21} j'_l(\kappa_2 r_1) n_l(\kappa_1 r_1) - j_l(\kappa_2 r_1) n'_l(\kappa_1 r_1)] \end{bmatrix} \quad (\text{where } c \equiv \kappa_2 r_1^2 / \beta_{21})
 \end{aligned} \tag{A36}$$

These expressions put in the form of Eq. (A25) yield

$$t_{11}^{(2)} = c[\beta_{21} n'_l(\kappa_2 r_1) j_l(\kappa_1 r_1) - n_l(\kappa_2 r_1) j'_l(\kappa_1 r_1)], \tag{A37}$$

$$t_{21}^{(2)} = -c[\beta_{21} j'_l(\kappa_2 r_1) j_l(\kappa_1 r_1) - j_l(\kappa_2 r_1) j'_l(\kappa_1 r_1)]. \tag{A38}$$

Substituting Eqs. (A37) and (A38) into Eq. (A33), we obtain the Green function for a bi-layered spherical structure which is identical to that derived in Ref. 9, as expected.

Similarly, for the impulse response, from Eq. (A23), we can obtain

$$\begin{bmatrix} a_N \\ b_N \end{bmatrix} = T_{N-1} T_{N-2} \cdots T_{j+1} T_j \begin{bmatrix} a_j \\ b_j \end{bmatrix}. \tag{A39}$$

Then

$$\begin{bmatrix} a_j \\ b_j \end{bmatrix} = T_j^{-1} T_{j+1}^{-1} \cdots T_{N-1}^{-1} T_N^{-1} \begin{bmatrix} a_N \\ b_N \end{bmatrix}. \tag{A40}$$

We can write out the matrix  $T_j^{-1} T_{j+1}^{-1} \cdots T_{N-1}^{-1} T_N^{-1}$ , in the form

$$T_j^{-1} T_{j+1}^{-1} \cdots T_{N-1}^{-1} T_N^{-1} \equiv \begin{bmatrix} w_{11}^{(j)}, w_{12}^{(j)} \\ w_{21}^{(j)}, w_{22}^{(j)} \end{bmatrix}. \tag{A41}$$

So

$$a_j = w_{11}^{(j)} a_N + w_{12}^{(j)} b_N, \tag{A42}$$

$$b_j = w_{21}^{(j)} a_N + w_{22}^{(j)} b_N. \tag{A43}$$

Also

$$h_{jl}(r, r_0; \omega) = a_j j_l(\kappa_j r) + b_j n_l(\kappa_j r). \tag{A44}$$

Now the solution can be written as

$$\begin{aligned}
 h_{jl}(r, r_0; \omega) &= (w_{11}^{(j)} a_N + w_{12}^{(j)} b_N) j_l(\kappa_j r) \\
 &\quad + (w_{21}^{(j)} a_N + w_{22}^{(j)} b_N) n_l(\kappa_j r).
 \end{aligned} \tag{A45}$$

Then the spatial impulse-response function of region  $j$  becomes

$$\begin{aligned}
 H_j(\vec{r}|\vec{r}_0; \omega) &= \frac{1}{2\pi} \sum_{l=0}^{\infty} [(w_{11}^{(j)} a_N + w_{12}^{(j)} b_N) j_l(\kappa_j r) \\
 &\quad + (w_{21}^{(j)} a_N + w_{22}^{(j)} b_N) n_l(\kappa_j r)] \cdot N_l(\theta) N_l(\theta_0).
 \end{aligned} \tag{A46}$$

**2. Equivalence relation between a multi-layer composite sphere with homogeneous Neumann conditions at the exterior surface of region N ( $r=r_N$ ) (Sec. I) and a hollow sphere with a homogeneous Neumann condition at  $r=b \rightarrow r_N$  (exterior surface), namely  $m_2=0$ , and a homogeneous third-kind boundary condition at interior surface of a hollow sphere  $r=a \rightarrow r_{N-1}$**

In Sec. I, the Green function, Eq. (A33), evaluated at  $r = r_{N-1}$  can be re-arranged as follows:

$$\begin{aligned}
 G^{(N)}(\vec{r}_{N-1}|\vec{r}_0; \omega) &= \frac{\kappa_N}{2\pi\alpha_N} \sum_{l=0}^{\infty} g^{(N)}(r_1, r_2, \cdots, r_N, r_{N-1}) \\
 &\quad \cdot [j_l(\kappa_N r_0) n'_l(\kappa_N r_N) - j'_l(\kappa_N r_N) n(\kappa_N r_0)] \\
 &\quad \times N_l(\theta) \cdot N_l(\theta_0),
 \end{aligned} \tag{A47}$$

where  $g^{(N)}(r_1, r_2, \cdots, r_{N-1}, r_N) = \frac{j_l(\kappa_N r_{N-1}) t_{11}^{(N)} + n_l(\kappa_N r_{N-1}) t_{21}^{(N)}}{j'_l(\kappa_N r_N) t_{11}^{(N)} + n'_l(\kappa_N r_N) t_{21}^{(N)}}$ .

The quantities  $t_{11}^{(N)}$  and  $t_{21}^{(N)}$  can be determined from

$$\begin{bmatrix} t_{11}^{(N)} \\ t_{21}^{(N)} \end{bmatrix} = T_{N-1} \begin{bmatrix} t_{11}^{(N-1)} \\ t_{21}^{(N-1)} \end{bmatrix}, \tag{A48}$$

where

$$\begin{aligned}
 T_{N-1} &= B_{N-1}^{-1} A_{N-1} \\
 &= \frac{\kappa_N r_{N-1}^2}{\beta_{N,N-1}} \begin{bmatrix} \beta_{N,N-1} n'_l(\kappa_N r_{N-1}), -n_l(\kappa_N r_{N-1}) \\ -\beta_{N,N-1} j'_l(\kappa_N r_{N-1}), j_l(\kappa_N r_{N-1}) \end{bmatrix}.
 \end{aligned} \tag{A49}$$

Furthermore,

---


$$\begin{aligned}
 &\begin{bmatrix} j_l(\kappa_{N-1} r_{N-1}), n_l(\kappa_{N-1} r_{N-1}) \\ j'_l(\kappa_{N-1} r_{N-1}), n'_l(\kappa_{N-1} r_{N-1}) \end{bmatrix} \\
 &= c \begin{bmatrix} \beta_{N,N-1} n'_l(\kappa_N r_{N-1}) j_l(\kappa_{N-1} r_{N-1}) - n_l(\kappa_N r_{N-1}) j'_l(\kappa_{N-1} r_{N-1}), & \beta_{N,N-1} n'_l(\kappa_N r_{N-1}) n_l(\kappa_{N-1} r_{N-1}) - n_l(\kappa_N r_{N-1}) n'_l(\kappa_{N-1} r_{N-1}) \\ -[\beta_{N,N-1} j'_l(\kappa_N r_{N-1}) j_l(\kappa_{N-1} r_{N-1}) - j_l(\kappa_N r_{N-1}) j'_l(\kappa_{N-1} r_{N-1})], & -[\beta_{N,N-1} j'_l(\kappa_N r_{N-1}) n_l(\kappa_{N-1} r_{N-1}) - j_l(\kappa_N r_{N-1}) n'_l(\kappa_{N-1} r_{N-1})] \end{bmatrix},
 \end{aligned} \tag{A50}$$

where  $c \equiv \kappa_N r_{N-1}^2 / \beta_{N,N-1}$ .  
Combining results,

$$j_l(\kappa_N r_{N-1}) t_{11}^{(N)} + n_l(\kappa_N r_{N-1}) t_{21}^{(N)} = \frac{c}{\kappa_N r_{N-1}^2} \beta_{N,N-1} [j_l(\kappa_{N-1} r_{N-1}) t_{11}^{(N-1)} + n_l(\kappa_{N-1} r_{N-1}) t_{21}^{(N-1)}]. \tag{A51}$$

Similarly we find

$$j'_l(\kappa_N r_N) t_{11}^{(N)} + n'_l(\kappa_N r_N) t_{21}^{(N)} = c \{ \beta_{N,N-1} [j_l(\kappa_{N-1} r_{N-1}) t_{11}^{(N-1)} + n_l(\kappa_{N-1} r_{N-1}) t_{21}^{(N-1)}] [j'_l(\kappa_N r_N) n'_l(\kappa_N r_{N-1}) - j'_l(\kappa_N r_{N-1}) n'_l(\kappa_N r_N)] \\ + [j'_l(\kappa_{N-1} r_{N-1}) t_{11}^{(N-1)} + n'_l(\kappa_{N-1} r_{N-1}) t_{21}^{(N-1)}] [j_l(\kappa_N r_{N-1}) n'_l(\kappa_N r_N) - j'_l(\kappa_N r_N) n_l(\kappa_N r_{N-1})] \}. \tag{A52}$$

Collecting terms

$$G^{(N)}(\vec{r}_{N-1} | \vec{r}_0; \omega) = \frac{\kappa_N}{2\pi\alpha_N} \sum_{l=0}^{\infty} N_l(\theta) N_l(\theta_0) \\ \times \frac{[j_l(\kappa_N r_0) n'_l(\kappa_N r_N) - n_l(\kappa_N r_0) j'_l(\kappa_N r_N)] / (\kappa_N r_{N-1}^2)}{[j'_l(\kappa_N r_N) n'_l(\kappa_N r_{N-1}) - j'_l(\kappa_N r_{N-1}) n'_l(\kappa_N r_N)] + \lambda [j_l(\kappa_N r_{N-1}) n'_l(\kappa_N r_N) - j'_l(\kappa_N r_N) n_l(\kappa_N r_{N-1})]}, \tag{A53}$$

where

$$\lambda \equiv \frac{[j'_l(\kappa_{N-1} r_{N-1}) t_{11}^{(N-1)} + n'_l(\kappa_{N-1} r_{N-1}) t_{21}^{(N-1)}]}{\beta_{N,(N-1)} [j_l(\kappa_{N-1} r_{N-1}) t_{11}^{(N-1)} + n_l(\kappa_{N-1} r_{N-1}) t_{21}^{(N-1)}]}. \tag{A54}$$

For a hollow sphere, the Green function in the region N can be expressed as<sup>9</sup>

$$G(\vec{r}_{N-1} | \vec{r}_0; \omega) = \frac{\kappa_N}{2\pi\alpha_N} \sum_{l=0}^{\infty} N_l(\theta) N_l(\theta_0) \\ \times \frac{[j_l(\kappa_N r_0) n'_l(\kappa_N r_N) - n_l(\kappa_N r_0) j'_l(\kappa_N r_N)] / (\kappa_N r_{N-1}^2)}{[j'_l(\kappa_N r_N) n'_l(\kappa_N r_{N-1}) - j'_l(\kappa_N r_{N-1}) n'_l(\kappa_N r_N)] + m_{(N-1)} [j_l(\kappa_N r_{N-1}) n'_l(\kappa_N r_N) - j'_l(\kappa_N r_N) n_l(\kappa_N r_{N-1})]}. \tag{A55}$$

Comparing with Eq. (A53), it is found that

$$m_{(N-1)} \equiv \frac{h_{(N-1)}}{k_N} \tag{A58}$$

$$m_{(N-1)} = \lambda \\ = \frac{[j'_l(\kappa_{N-1} r_{N-1}) t_{11}^{(N-1)} + n'_l(\kappa_{N-1} r_{N-1}) t_{21}^{(N-1)}]}{\beta_{N,(N-1)} [j_l(\kappa_{N-1} r_{N-1}) t_{11}^{(N-1)} + n_l(\kappa_{N-1} r_{N-1}) t_{21}^{(N-1)}]}, \\ (N \geq 2). \tag{A56}$$

between  $m_{(N-1)}$  and the effective heat transfer coefficient  $h_{(N-1)}$ ,<sup>15</sup> we find

$$h_{(N-1)} = k_{(N-1)} \cdot \frac{[j'_l(\kappa_{N-1} r_{N-1}) + n'_l(\kappa_{N-1} r_{N-1}) \gamma_{(N-1)}]}{[j_l(\kappa_{N-1} r_{N-1}) + n_l(\kappa_{N-1} r_{N-1}) \gamma_{(N-1)}]}. \tag{A59}$$

Using definitions Eqs. (A25a) and (A13a),  $m_{(N-1)}$  can be written in the form

If  $N = 2$ , Eq. (A57) reduces to Ref. 6, Eq. (A.3.4)

$$m_{(N-1)} = \frac{[j'_l(\kappa_{N-1} r_{N-1}) + n'_l(\kappa_{N-1} r_{N-1}) \gamma_{(N-1)}]}{\beta_{N,(N-1)} [j_l(\kappa_{N-1} r_{N-1}) + n_l(\kappa_{N-1} r_{N-1}) \gamma_{(N-1)}]}. \tag{A57}$$

$$h_1 = k_1 \cdot \frac{j'_l(\kappa_1 r_1) + n'_l(\kappa_1 r_1) \gamma_1}{j_l(\kappa_1 r_1) + n_l(\kappa_1 r_1) \gamma_1} = k_1 \frac{j'_l(\kappa_1 r_1)}{j_l(\kappa_1 r_1)}, \quad (\gamma_1 \equiv 0). \tag{A60}$$

Now turning to the relation

As expected, on replacing the otherwise arbitrary constants  $m_{(N-1)}$  and  $h_{(N-1)}$  in Eq. (A55) with the foregoing expressions which contain thermal-wave parameters from the

underlayer region  $N - 1$ , the Green function (A33) can be transformed into a proper Green function for region  $N$ . As such, Equations (A55) with Eqs. (A57) and (A59) satisfy the field equations (6) and (7) with those particular values of  $m_{(N-1)}$  and  $h_{(N-1)}$ . Substituting  $m_{(N-1)}$  and  $h_{(N-1)}$  into Eq. (A59), one can obtain the Green function in region  $N$ , and on using in Eq. (5)  $F_N(\vec{r}_N^s, \omega)$  from Eq. (12), the thermal-wave field, Eq. (14), is obtained in region  $N$  after some algebraic manipulation.

<sup>1</sup>*Non-Destructive Evaluation: Progress in Photothermal and Photoacoustic Science and Technology*, edited by A. Mandelis (PTR-Prentice Hall, Englewood Cliffs, NJ, 1994), Vol. 2.

<sup>2</sup>H. K. Park, C. P. Grigoropoulos, and A. C. Tam, *Int. J. Thermophys.* **16**, 973 (1995).

<sup>3</sup>R. Santos and L. C. M. Miranda, *J. Appl. Phys.* **52**, 4194 (1981).

<sup>4</sup>D. P. Almond and P. M. Patel, *Photothermal Science and Techniques* (Chapman and Hall, London, 1996).

<sup>5</sup>L. Fabbri and P. Fenici, *Rev. Sci. Instrum.* **66**, 3593 (1995).

<sup>6</sup>C. Wang, A. Mandelis, and Y. Liu, *J. Appl. Phys.* **96**, 3756 (2004).

<sup>7</sup>C. Wang and A. Mandelis, *Rev. Sci. Instrum.* **78**, 054902 (2007).

<sup>8</sup>C. Wang, Y. Liu, A. Mandelis, and J. Shen, *J. Appl. Phys.* **101**, 083503 (2007).

<sup>9</sup>G. Xie, Z. Chen, C. Wang, and A. Mandelis, *Rev. Sci. Instrum.* **80**, 0349031 (2009).

<sup>10</sup>G. Xie, J. Zhang, L. Liu, C. Wang, and A. Mandelis, *J. Appl. Phys.* **109**, 113534 (2011).

<sup>11</sup>A. Salazar, F. Garrido, and R. Celorrio, *J. Appl. Phys.* **99**, 066116 (2006).

<sup>12</sup>A. Salazar and R. Celorrio, *J. Appl. Phys.* **100**, 113535 (2006).

<sup>13</sup>N. Madariaga and A. Salazar, *J. Appl. Phys.* **101**, 103534 (2007).

<sup>14</sup>H. Qu, C. Wang, X. Guo, and A. Mandelis, *J. Appl. Phys.* **104**, 113518 (2008).

<sup>15</sup>A. Mandelis, *Diffusion-Wave Fields: Mathematical Methods and Green Functions* (Springer, New York, 2001), pp. 85, 90, and 200.

<sup>16</sup>R. E. Imhof, B. Zhang, and D. J. S. Birch, "Photothermal radiometry for NDE," in *Progress in Photothermal and Photoacoustic Science and Technology: Non-Destructive Evaluation* (PTR Prentice-Hall, Englewood Cliffs, NJ, 1994), Chap. 7, Vol. 2.

<sup>17</sup>R. Steiner, "Properties of selection: Iron, steel of high performance alloys," in *Metals Handbook*, 10th ed. (ASM International, Material Park, Ohio, 1990), Vol. 1, p. 196.

<sup>18</sup>A. Mandelis, F. Funak, and M. Munidasa, *J. Appl. Phys.* **80**, 5570 (1996).